



# A poro-viscoplastic constitutive model for cold compacted powders at finite strains

A. Krairi<sup>a</sup>, K. Matouš<sup>a,b,\*</sup>, A. Salvadori<sup>a,b</sup>

<sup>a</sup> Center for Shock Wave-processing of Advanced Reactive Materials (C-SWARM), University of Notre Dame, Notre Dame, IN, 46556, USA

<sup>b</sup> Department of Aerospace and Mechanical Engineering, University of Notre Dame, Notre Dame, IN, 46556, USA



## ARTICLE INFO

### Article history:

Received 14 November 2016

Revised 1 June 2017

Available online 5 December 2017

### Keywords:

Cold compacted media

Metal powders

Finite strains

Visco-plastic rate-dependent model

Elasto-plastic coupling

Pressure sensitivity

## ABSTRACT

A novel finite strain poro-viscoplastic phenomenological model for cold compacted materials is proposed. The model relies on the three-stage density evolution paradigm and describes the material evolution from loose to solid state. This model accounts for rate dependence, elasto-plastic coupling, pressure sensitivity, and transition to full solid state. The model has been implemented, verified, and validated against experimental data available in the literature for copper powder compounds.

© 2017 Elsevier Ltd. All rights reserved.

## 1. Introduction

Modeling granular materials is an important and challenging task, which is needed for several applications. These include applications in the pharmaceutical industry (Muzzio et al., 2002), powder metallurgy (German, 2005), ceramics (Glass and Ewsuk, 1997), soil mechanics (Iwashita and Oda, 1999), and many others. Overall (effective) chemical and mechanical properties arise from microstructural processes, which occur at the particles scale. Processing options permit selective placement of phases or pores to achieve targeted effective properties. For instance, mixing two or more metal or ceramic powders and exposing them to specific pressure and temperature conditions may lead to material synthesis. An example of this is the use of high energy ball milling to obtain reactive metallic composites (i.e. Shuck et al., 2016).

In this work, we focus mainly on metal/ceramic powders. Components made with metal/ceramic powders are produced by cold or hot compaction (see Cocks, 2001 for a detailed description of the manufacturing process). During the compaction, the applied pressure controls the change in the material's elastic and strength properties. It is commonly accepted that the transition from loose state to full solid state is defined by three stages (eg. Piccolroaz et al., 2006a): stage I corresponds to granule sliding and rearrangement, stage II is characterized by granule deformation,

and stage III is dominated by granule densification and hardening (see Fig. 1).

In order to capture the behavior described above, both microscopic and macroscopic approaches have been proposed (Bier et al., 2007). In the microscopic approach, the grains are often modeled as spherical with different assumptions concerning the contact between them (Arzt, 1982; Cocks and Sinka, 2007). In the work of Fleck, Cocks, and co-workers (Fleck et al., 1992; Fleck, 1995; Ogbonna and Fleck, 1995; Fleck et al., 1997; Sridhar and Fleck, 2000; Cocks, 2001; Cocks and Sinka, 2007; Sinka and Cocks, 2007), several plastic and viscoplastic compaction models have been built based on an ensemble of spherical particles. Heyliger and McMeeking (2001) modeled the material as a network of axial forces rotated in space and predicted the overall rate independent stress-strain behavior under cold compaction. Micro-mechanical approaches provide insights on the complex physics of cold compaction. For example, numerical simulations in representative unit cells, as in Yi et al. (2005), highlighted the role of inter-particle friction and particle failure during compaction. However, these methods at this stage are unsuitable to simulate large problems of industrial interest due to their excessive computational complexity.

Phenomenological approaches at a macroscopic scale can cover a larger range of relative densities. A vast amount of literature has been proposed to this aim, based on the concept of a pressure dependent yield function (Bigoni and Piccolroaz, 2004), conceptually similar to the well known Cam-Clay (Schofield and Wroth, 1968) and Drucker-Prager (Drucker and Prager, 1952)

\* Corresponding author at: Department of Aerospace and Mechanical Engineering, University of Notre Dame, Notre Dame, IN, 46556, USA.

E-mail address: [kmatous@nd.edu](mailto:kmatous@nd.edu) (K. Matouš).

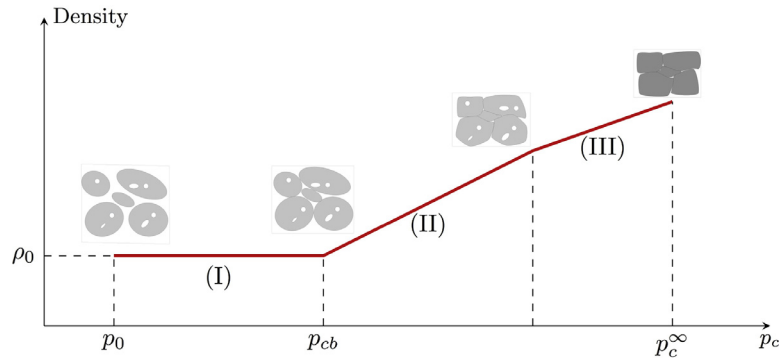


Fig. 1. Illustration of the material density evolution as a function of the consolidation pressure. Stage I - granule sliding and rearrangement. Stage II - granule deformation. Stage III - granule densification and hardening.  $p_0$  and  $\rho_0$  are the initial pressure and initial density, respectively.  $p_{cb}$  is the forming pressure corresponding to the transition from the stage I to stage II.  $p_c^\infty$  is the pressure needed to reach the full solid state.

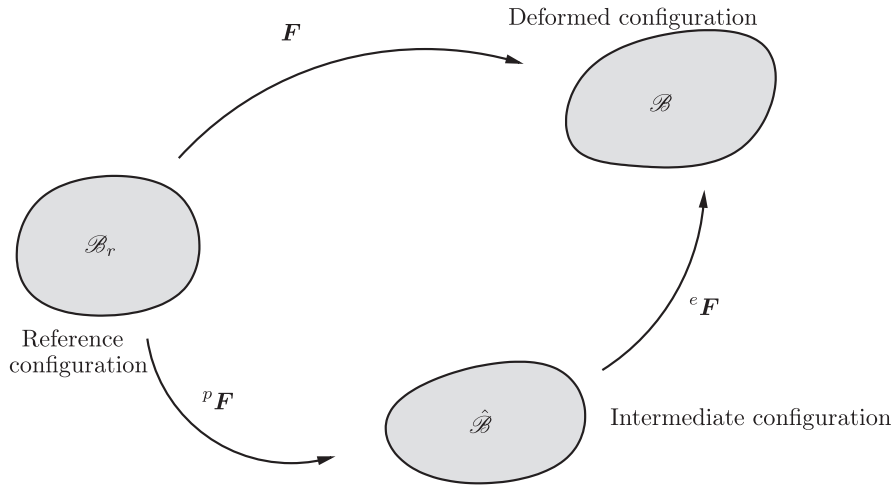


Fig. 2. Reference, current and intermediate configurations.

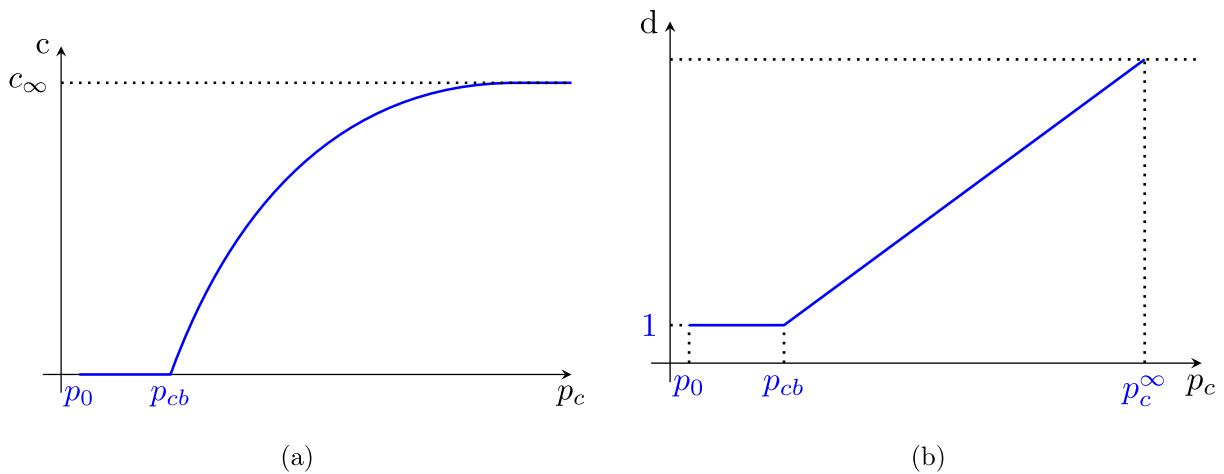


Fig. 3. Illustration of  $c(p_c)$  and  $d(p_c)$  as a function of  $p_c$ .

models in soil mechanics. Near the full dense state, yield functions such as the Gurson's (Gurson, 1977) are often used. Specific yield functions for metal powders have been developed by Kuhn and Downey (1971) and Shima and Oyane (1976). In order to capture the complex and variable evolution of the yield surface with the confining pressure, two approaches are mainly used (Bier and Hartmann, 2006): the Cap-yield functions and shape flexible yield functions. Cap-yield functions (e.g. Watson

and Wert, 1993; Coube and Riedel, 2000; Gu et al., 2001; Khoei and Azami, 2005; Bier and Hartmann, 2006) employ an interpolation of two or more recognized yield functions to construct yield surfaces with complex shape. Rather than combining different expressions, shape flexible yield functions make use of a single map, usually defined in Lode coordinates, whose evolution in time is governed by internal variables. Examples of flexible shape yield functions are given in Ehlers (1995),

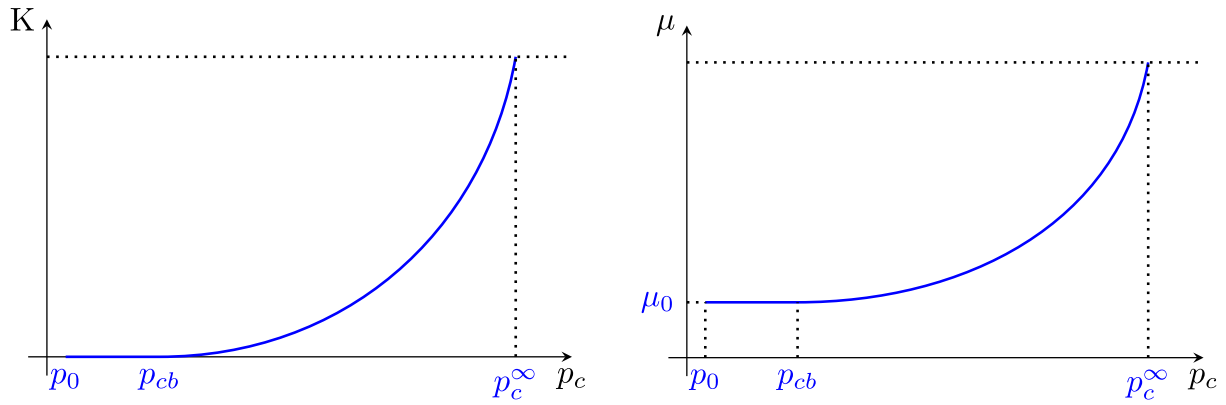


Fig. 4. Illustration of  $\mu(p_c)$  and  $K(p_c)$  as a function of  $p_c$ .

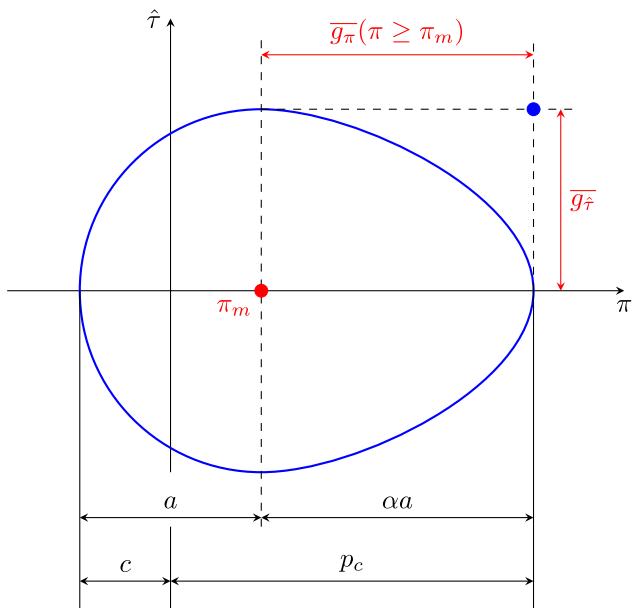


Fig. 5. Illustration of the Cam-Clay yield surface in  $(\pi, \tau)$  plane. Here we illustrate the construction of hardening functions  $\bar{g}_\pi$  and  $\bar{g}_\tau$ .

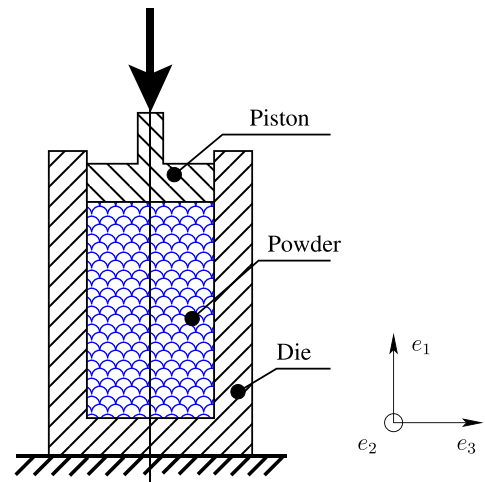


Fig. 6. Die compaction test to calibrate the material data in Table 1.

Gu et al. (2001), Bigoni and Piccolroaz (2004), Aubertin and Li (2004), Piccolroaz and Bigoni (2009) and Bennett et al. (2016). Generally, they require several additional material parameters.

Endochronic models for cold compacted materials also exist (Hägglblad, 1991; Khoei et al., 2002; Bakhshiani et al., 2004). This theory does not employ a yield function to model inelastic behaviors. It has been developed initially in the realm of plastic behavior of metals (Valanis, 1971) and extended to the inelastic behavior of concrete and soils (eg. Bažant et al., 1976).

Several approaches mentioned above are formulated under the assumption of small strains. Additionally, they generally only focus on modeling the pressure dependence of the material. Moreover, the rate dependence is generally ignored, except when the material is heated (i.e. in hot-pressing of metal powders). Under cold compaction, rate sensitivity is generally neglected. Depending on the grain material and/or the manufacturing processes (e.g. use of lubrication), the material response may exhibit a rate dependence during or after compaction (e.g. Wei and Anand, 2007). In addition, the transition to the full solid state is generally unaccounted for.

In this work, we propose a new phenomenological finite strain macroscopic model, which couples pressure sensitivity and rate

dependence of cold compacted materials. It allows modeling of the change in the material elastic properties. The progressive transition from loose powder to full solid state is modeled by a compaction function. As the state approaches the full solid state, the material becomes less sensitive to pressure and irreversible volumetric deformations become very small. The proposed flow rule is expressed using the Kirchhoff stress state similarly to existing large deformations viscoplastic and viscoelastic formulations (e.g. Matouš and Maniatty, 2004; Wei and Anand, 2007; Areias and Matouš, 2008). Careful model calibration and independent validation studies are provided.

The paper is organized as follows. The constitutive theory is detailed in Section 2, the numerical integration algorithm is given in Section 3, and Section 4 contains parameter calibration, experimental validations, and numerical simulations that highlight the model features and capabilities. Finally, conclusions are given in Section 5.

## 2. Constitutive theory

In this work, the description of the transformation from a reference configuration,  $\mathcal{B}_r$ , to a deformed configuration,  $\mathcal{B}$ , is given by a motion  $\phi(\mathbf{X}, t)$ . Here  $\mathbf{X} \in \mathbb{R}^3$  designates the position of a particle in the reference configuration and  $t \in \mathbb{R}^+$  is the time. Let  $\mathbf{F}(\mathbf{X}, t) = \nabla \phi(\mathbf{X}, t)$  be the total deformation gradient at  $\mathbf{X}$  and  $t$ , where symbol  $\nabla$  denotes the gradient with respect to  $\mathbf{X}$ . An intermediate or relaxed configuration,  $\hat{\mathcal{B}}$ , (see Fig. 2) is introduced in

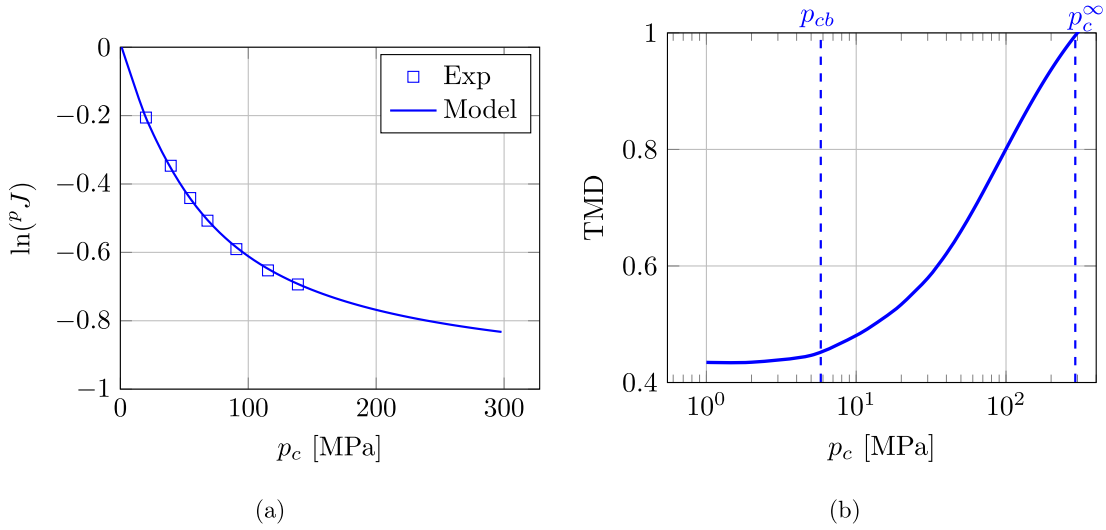


Fig. 7. (a) Plastic volumetric strain as a function of the forming pressure  $p_c$ . (b) TMD as a function of  $p_c$ . Experimental data are taken from Bier et al. (2007).

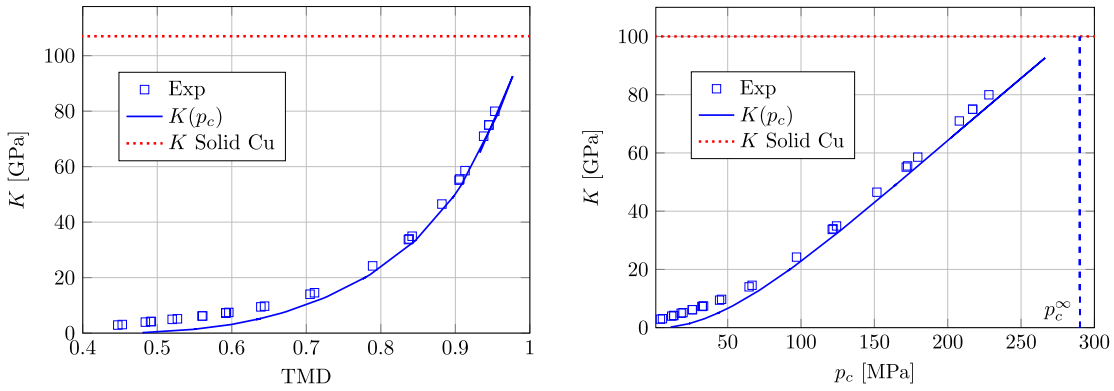


Fig. 8. Evolution of  $K$  as a function of TMD and  $p_c$ . Experimental data are from Carnavas and Page (1998).

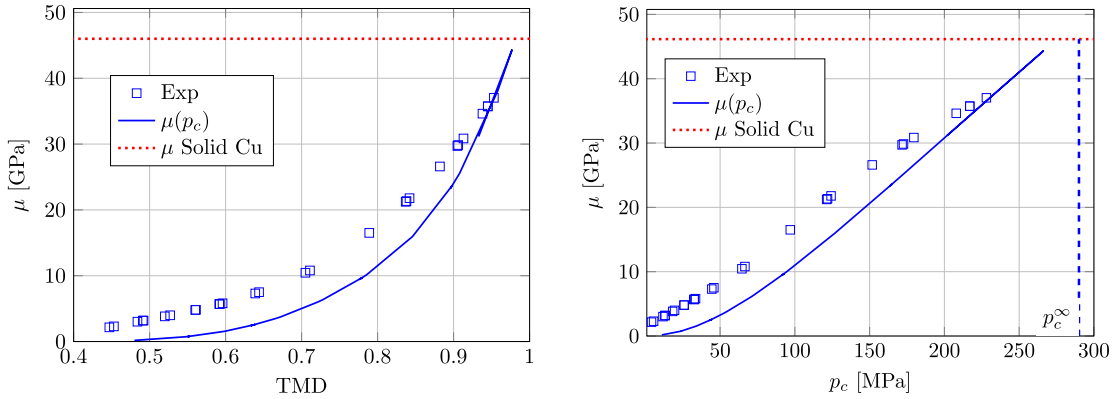


Fig. 9. Evolution of the shear modulus as a function of TMD and  $p_c$ . Experimental data are from Carnavas and Page (1998).

order to decompose the deformation gradient  $\mathbf{F}$  into its elastic  ${}^e\mathbf{F}$  and plastic  ${}^p\mathbf{F}$  parts, (Kröner, 1959 and Lee, 1969):

$$\mathbf{F} = {}^e\mathbf{F} {}^p\mathbf{F}. \quad (1)$$

The total  $\mathbf{C}$ , plastic  ${}^p\mathbf{C}$ , and elastic  ${}^e\mathbf{C}$  right Cauchy-Green tensors are defined as:

$$\mathbf{C} = \mathbf{F}^T \mathbf{F}, \quad {}^p\mathbf{C} = {}^p\mathbf{F}^T {}^p\mathbf{F}, \quad {}^e\mathbf{C} = {}^e\mathbf{F}^T {}^e\mathbf{F}. \quad (2)$$

The volumetric strains used in the formulation are

$$J = \det \mathbf{F}, \quad {}^pJ = \det {}^p\mathbf{F}, \quad {}^eJ = \det {}^e\mathbf{F}, \quad (3)$$

with  $J = {}^eJ {}^pJ$ . The densities in the current ( $\rho$ ), intermediate ( $\hat{\rho}$ ), and reference ( $\rho_0$ ) configurations are linked by the following identities:

$$\rho = \frac{\rho_0}{J} = \frac{\hat{\rho}}{{}^eJ}, \quad \hat{\rho} = \frac{\rho_0}{{}^pJ}. \quad (4)$$

### 2.1. Free energy density function

In order to capture the complicated physics presented in the introduction, we propose a modification of the free en-

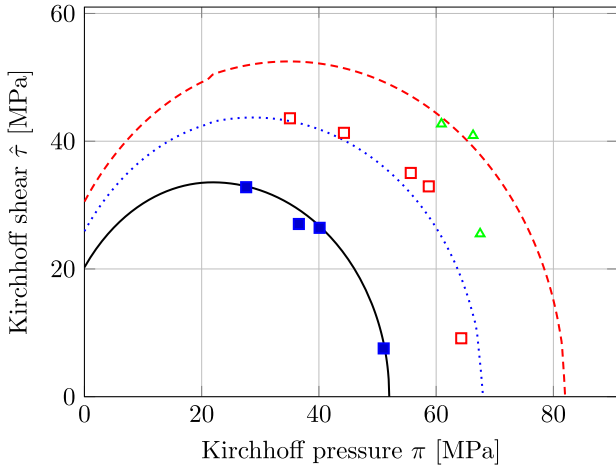


Fig. 10. Yield surfaces for different values of forming pressure  $p_c$ . Experimental data are taken from Carnavas (1996).

ergy density introduced by Piccolroaz et al. (2006a, 2006b) and Stupkiewicz et al. (2015). The modified expression, which connotes an isotropic material behavior, reads

$$W({}^e\mathbf{C}, p_c) = \hat{W}({}^e\mathbf{C}, p_c) + U({}^eJ, p_c), \quad (5)$$

where  $\hat{W}({}^e\mathbf{C}, p_c)$  denotes the volume preserving part of the energy and  $U({}^eJ, p_c)$  represents the volumetric part. Here,  $p_c$  is a monotonically increasing internal state variable, physically interpreted as the forming pressure at which the powder was compacted until current time. The isochoric behavior is described by the function

$$\hat{W}({}^e\mathbf{C}, p_c) = \frac{1}{2} \mu(p_c) [{}^eJ^{-2/3} \text{tr}({}^e\mathbf{C}) - 3], \quad (6)$$

which corresponds to the classical neo-Hookean model with the shear modulus  $\mu$  as a function of  $p_c$ . The expression of the shear modulus  $\mu(p_c)$  reads

$$\mu(p_c) = \mu_0 + c(p_c) \left[ d(p_c) - \frac{1}{d(p_c)} \right] \mu_1, \quad (7)$$

where  $\mu_0, \mu_1$  are constant material parameters. In our work, cohesion,  $c(p_c)$ , identifies the tensile strength of the powder. The cohesion  $c$  and the transition function  $d$  depend on the forming pressure  $p_c$  through the following expressions

$$c(p_c) = c_\infty [1 - \exp(-\Gamma \langle p_c - p_{cb} \rangle)], \quad (8)$$

$$d(p_c) = 1 + B \langle p_c - p_{cb} \rangle, \quad (9)$$

where  $c_\infty, \Gamma, p_{cb}$  and  $B$  are additional material parameters.  $c_\infty$  is the saturation value of the cohesion and  $p_{cb}$  is the value of  $p_c$  corresponding to the transition from stage I to stage II (see Fig. 3(a)). The symbol  $\langle \cdot \rangle$  denotes the Macaulay brackets. Function  $d$  is a measure of the granule deformation and densification. It holds unity at forming pressure less than  $p_{cb}$ , whereas at complete compaction  $d \gg 1$  (see Fig. 3(b)).

The volumetric part of the free energy,  $U({}^eJ, p_c)$ , is a function of  $p_c$  by means of the cohesion,  $c$ , and of the bulk modulus like variable,  $K$ :

$$U({}^eJ, p_c) = \frac{1}{2} K(p_c) ({}^eJ - 1) \ln({}^eJ) + \left\{ c \ln({}^eJ) + [p_0 + c] \times \left( \frac{c_\infty}{c_\infty - c} \right)^n \kappa \exp \left( -\frac{\ln({}^eJ)}{\kappa} \left( \frac{c_\infty - c}{c_\infty} \right)^n \right) \right\}. \quad (10)$$

The expression of  $K(p_c)$  reads

$$K(p_c) = [p_0 + c(p_c)] \left[ d(p_c) - \frac{1}{d(p_c)} \right] \frac{1}{\kappa}. \quad (11)$$

Here,  $p_0$  is the initial pressure and  $\kappa$  is the logarithmic bulk modulus. Figs. 3 and 4 give an illustration of  $\mu, K, c$ , and  $d$  as a function of the forming pressure  $p_c$ . The first contribution in Eq. (10) is standard (Doll and Schweizerhof, 2000): it models accurately the late stage II, and stage III when the material approaches a full solid. The term between curly brackets in Eq. (10) allows for modeling the material behavior in stage I and at the beginning of stage II, when the contribution of the cohesion dominates  $U({}^eJ, p_c)$ . In Piccolroaz et al. (2006a) a similar term inspired from the Cam-Clay model was present. Unfortunately, this introduced a nonlinear increase of elastic bulk modulus with mean pressure, a feature which is unrealistic during the late phase II of deformation. Such an issue does not arise using the volumetric part of the free energy in Eq. (10). In our work, we propose a new term that employs the cohesion as the controlling parameter. As the cohesion increases, the pressure related to the exponential term decreases and approaches  $p_0$  for  $c \rightarrow c_\infty$ . The parameter  $n$  in Eq. (10) controls the rate of decay of this part of the pressure response.

### 2.2. Visco-plastic flow rule

The plastic flow is assumed to be irrotational, and accordingly the evolution equation of  ${}^p\mathbf{F}$  is expressed as

$${}^p\dot{\mathbf{F}} = {}^p\mathbf{D} {}^p\mathbf{F}. \quad (12)$$

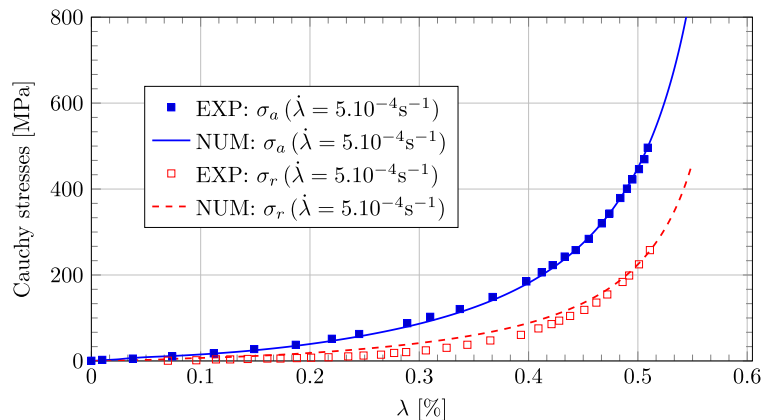
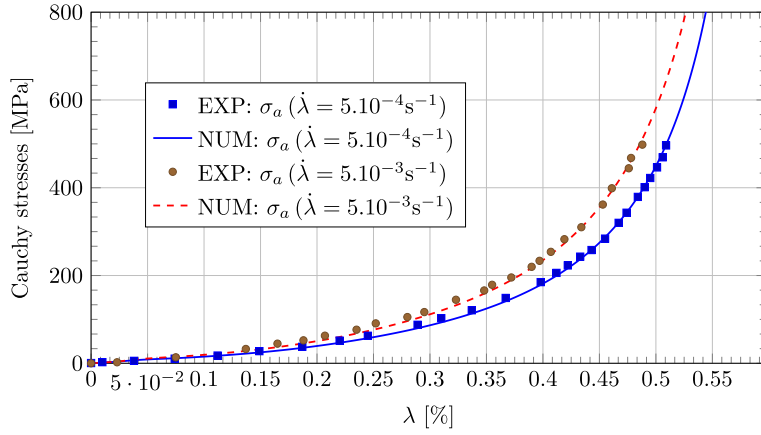
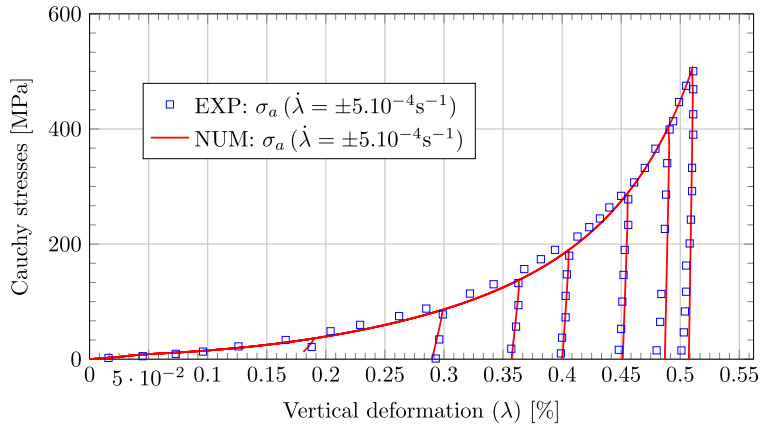


Fig. 11. Axial,  $\sigma_a$ , and radial,  $\sigma_r$ , Cauchy stress under monotonic loading rate  $\dot{\lambda} = 5.10^{-4} \text{s}^{-1}$ . Experimental data are taken from Bier et al. (2007) and  $\lambda$  is the strain measure in Eq. (27).



**Fig. 12.** Axial,  $\sigma_a$ , Cauchy stress under monotonic loading rates  $\dot{\lambda} = 5.10^{-4}\text{s}^{-1}$  and  $\dot{\lambda} = 5.10^{-3}\text{s}^{-1}$ . Experimental data are taken from Bier et al. (2007) and  $\lambda$  is the strain measure in Eq. (27).



**Fig. 13.** Axial,  $\sigma_a$ , Cauchy stress under loading-unloading at rate  $\dot{\lambda} = \pm 5.10^{-4}\text{s}^{-1}$ . Experimental data are taken from Bier et al. (2007).

The plastic stretching  ${}^p\mathbf{D}$  is decomposed into its deviatoric and volumetric parts as in Wei and Anand (2007)

$${}^p\mathbf{D} = {}^p\hat{\mathbf{D}} + \frac{1}{3}\text{tr}({}^p\mathbf{D})\mathbf{1}, \quad (13)$$

where the deviatoric part,  ${}^p\hat{\mathbf{D}}$ , reads

$${}^p\hat{\mathbf{D}} = \dot{\gamma}_d \text{dev}[\mathbf{S}]/\|\text{dev}[\mathbf{S}]\|_{\mathcal{F}}. \quad (14)$$

Here  $\dot{\gamma}_d = \|\dot{{}^p\hat{\mathbf{D}}}\|_{\mathcal{F}}$  is the equivalent plastic shear strain rate, and it is equal to the Frobenius norm<sup>1</sup> of  ${}^p\hat{\mathbf{D}}$ . The second Piola–Kirchhoff stress tensor,  $\mathbf{S}$ , is defined in the intermediate configuration (see Gurtin et al., 2010)

$$\mathbf{S} = 2 \frac{\partial W}{\partial \mathbf{e}\mathbf{C}} = 2 \frac{\partial \hat{W}}{\partial \mathbf{e}\mathbf{C}} - {}^e J p \mathbf{e}\mathbf{C}^{-1}, \quad (15)$$

with  $p = -\frac{\partial U}{\partial eJ}$  being the Cauchy pressure. The Cauchy stress,  $\boldsymbol{\sigma}$ , and the Kirchhoff stress,  $\boldsymbol{\tau}$ , are related to  $\mathbf{S}$  by

$$\boldsymbol{\sigma} = \frac{1}{eJ} {}^e \mathbf{F} \mathbf{S} {}^e \mathbf{F}^T, \quad \boldsymbol{\tau} = J \boldsymbol{\sigma}. \quad (16)$$

The volumetric part of  ${}^p\mathbf{D}$  evolves as

$$\text{tr}({}^p\mathbf{D}) = \beta_D \dot{\gamma}_v - \beta_C \dot{\gamma}_v, \quad (17)$$

where  $\dot{\gamma}_v$  is an equivalent plastic volumetric strain rate.  $\beta_C \geq 0$  is the compaction function and  $\beta_D \geq 0$  the shear-induced dilatancy

function. In particular,  $\beta_C$  controls the rate of compaction and vanishes when the material state is close to the full solid. We propose the following linear expression for  $\beta_C$  as a function of  $p_c$

$$\beta_C = g_0 \left(1 - \frac{p_c}{p_c^\infty}\right), \quad (18)$$

where  $g_0 \geq 0$  is a material parameter and  $p_c^\infty$  corresponds to the value of  $p_c$  at the full solid state. The shear-induced dilatancy function,  $\beta_D$ , is neglected in this work. An example for the dilatancy function may be found in Wei and Anand (2007).

The equivalent plastic strain rates  $\dot{\gamma}_d$  and  $\dot{\gamma}_v$  are specified by the power laws

$$\dot{\gamma}_v = \begin{cases} \dot{\gamma}_0 \left(\frac{\pi - \pi_m}{\bar{g}_\pi}\right)^{1/m} & \text{if } \pi > \pi_m \\ 0 & \text{otherwise,} \end{cases} \quad (19)$$

and

$$\dot{\gamma}_d = \dot{\gamma}_0 \left(1 - \frac{1}{d}\right) \left(\frac{\hat{\tau}}{\bar{g}_\tau}\right)^{1/m}, \quad (20)$$

where  $\dot{\gamma}_0$  is a reference plastic strain rate and  $m$  is the strain-rate sensitivity parameter. In our work, both parameters are assumed to be constant in time, as typical in the literature. Nevertheless, rate dependent laws incorporating this assumption can cover a large range of strain rates, see for instance Beaudoin and Acharya (2001).  $\pi$  is the Kirchhoff pressure,  $\hat{\tau}$  is the Frobenius norm of the deviatoric part of the Kirchhoff stress, and  $\pi_m$ ,  $\bar{g}_\pi$  and  $\bar{g}_\tau$  are functions

<sup>1</sup> The Frobenius norm of a tensor is defined as  $\|\mathbf{A}\|_{\mathcal{F}} = \sqrt{\mathbf{A} : \mathbf{A}}$ .

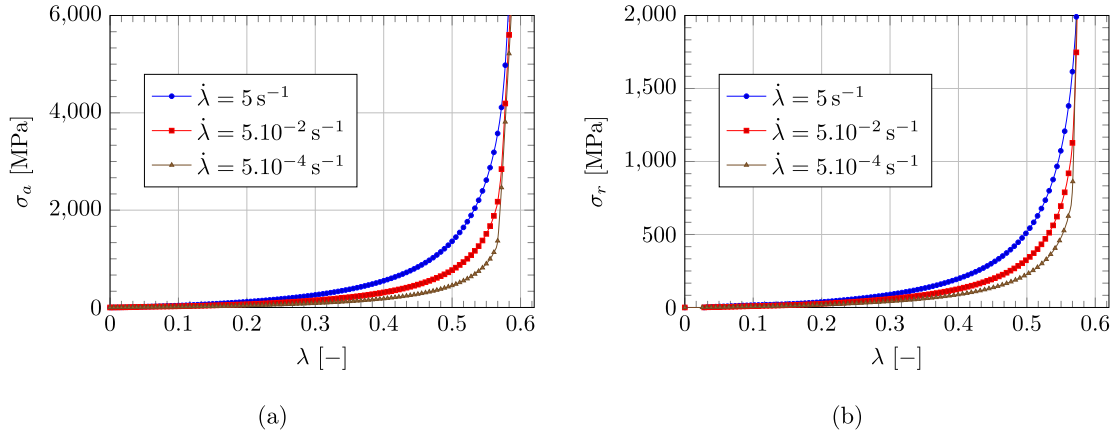


Fig. 14. Uniaxial constrained loading for different loading rates, until the full solid state, (a) Axial stress, (b) Radial stress.

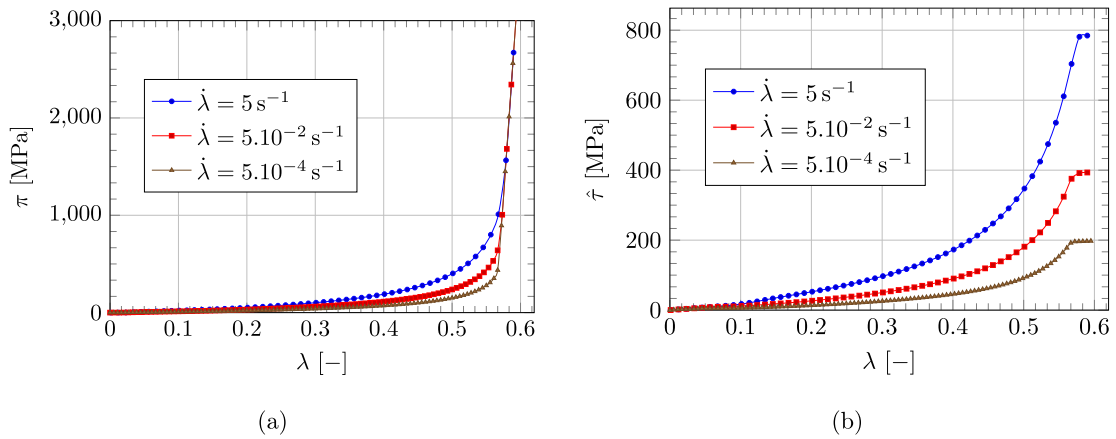


Fig. 15. Uniaxial constrained loading for different loading rates, until the full solid state. (a) Kirchhoff pressure, (b) The Frobenius norm of the deviatoric part of the Kirchhoff stress ( $\hat{\tau}$ ).

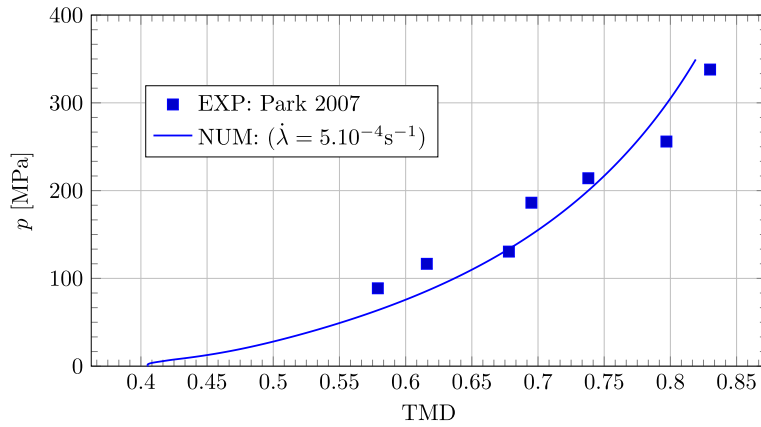


Fig. 16. Pressure in the copper powder under bi-axial compression test,  $TMD_0 = 0.405$ . Experimental data are taken from Park, (2007).

of  $p_c$  and play the role of hardening laws. These plastic strain rates are inspired by the modified Cam–Clay yield function expressed in the Kirchhoff stresses space (see Fig. 5):

$$\left(\frac{\pi - \pi_m}{\bar{g}_\pi}\right)^2 + \left(\frac{\hat{\tau}}{\bar{g}_\tau}\right)^2 = 1. \quad (21)$$

Here  $\bar{g}_\pi(p_c) = a(p_c)b$ ,  $\bar{g}_\tau(p_c) = \sqrt{\frac{3}{2}}a(p_c)M$ ,  $\pi_m(p_c) =$

$(a(p_c) - c(p_c))$  and

$$a(p_c) = \frac{p_c + c(p_c)}{1 + \alpha}, \quad b = \begin{cases} \alpha & \text{if } \pi \geq \pi_m \\ 1 & \text{if } \pi < \pi_m, \end{cases} \quad (22)$$

where  $M$  and  $\alpha$  are material parameters. Although the Cam–Clay yield function inspired some parameters (see Fig. 5), we note that our formulation does not use the yield function. Instead, we adopted a power-law evolution of the equivalent plastic strain rates  $\dot{\gamma}_d$  and  $\dot{\gamma}_v$  as in Wei and Anand (2007).

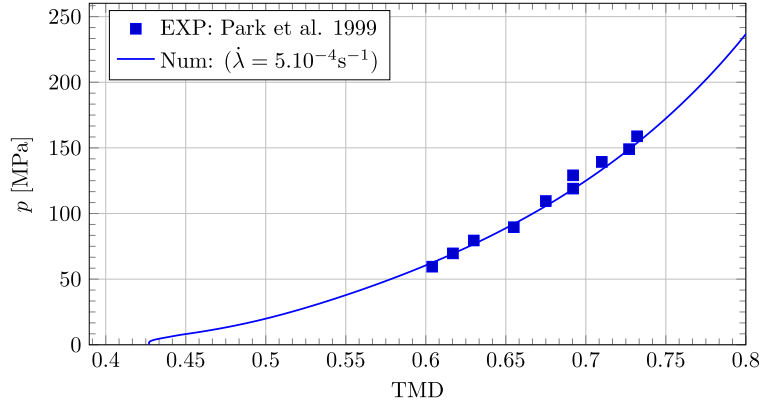


**Fig. 17.** Pressure in the copper powder under tri-axial compression test,  $TMD_0 = 0.427$  for coarse water-atomized Cu powder. Experimental data are taken from Park et al. (1999).

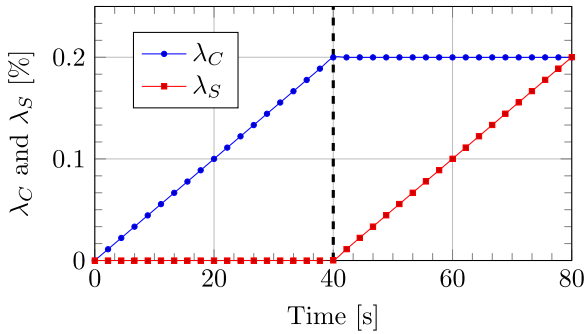


**Fig. 18.**  $\lambda_C$  and  $\lambda_S$  versus time for case 1.

### 2.3. Hardening law for $p_c$

The evolution of the internal variable  $p_c$  has been determined from the micromechanical model proposed by Cooper and Eaton (1962) (see also Piccolroaz et al., 2006a). It reads

$$\ln(p^J) = -a_1 \exp\left(-\frac{\Lambda_1}{p_c}\right) - a_2 \exp\left(-\frac{\Lambda_2}{p_c}\right), \quad (23)$$

where  $a_1$ ,  $\Lambda_1$ ,  $a_2$  and  $\Lambda_2$  are material parameters.

### 2.4. Theoretical Maximum Density (TMD)

A relationship can be established between the initial Theoretical Maximum Density,  $TMD_0$ , and the forming pressure required to

reach the full solid state,  $p_c^\infty$ . We denote with TMD the ratio between the density  $\hat{\rho}$  in the intermediate configuration, Eq. (4), and the density of the full solid material denoted henceforth with  $\rho_s$  (i.e., a material constant):

$$TMD = \frac{\hat{\rho}}{\rho_s}. \quad (24)$$

The former varies with the confining pressure, whereas the latter is taken constant. Assuming that the rise in densification begins at forming pressure  $p_c = p_{cb}$ , we have  $TMD_0 = TMD|_{p_{cb}}$ . Similarly, the full solid state is reached when  $\hat{\rho} = \rho_s$  at  $p_c = p_c^\infty$  (see Fig. 1). Thus, we conclude that  $TMD|_{p_c^\infty} = 1$  and  $p^J = p^J|_{p_c^\infty}$ . From the mass balance equation, we can derive:

$$TMD_0 = \frac{\rho_0}{\rho_s} = \frac{\hat{\rho}}{\rho_s} p^J = p^J TMD = p^J|_{p_c^\infty}. \quad (25)$$

Substituting (25) into Eq. (23), one has:

$$\ln[TMD_0] = -a_1 \exp\left(-\frac{\Lambda_1}{p_c^\infty}\right) - a_2 \exp\left(-\frac{\Lambda_2}{p_c^\infty}\right). \quad (26)$$

Accordingly, the material parameters  $p_c^\infty$ ,  $\Lambda_1$ ,  $\Lambda_2$ ,  $a_1$ , and  $a_2$  are not independent and must satisfy the constraint (26).

## 3. Numerical algorithm

In this section, we develop a simple numerical explicit integration algorithm for the proposed model (see Algorithm 1). Given the state of the system at time  $t_n$  and the increment of the total deformation  $\Delta F$ , the state at time  $t_{n+1} = t_n + \Delta t$  is computed using the Forward Euler method. The algorithm is summarized as follows:

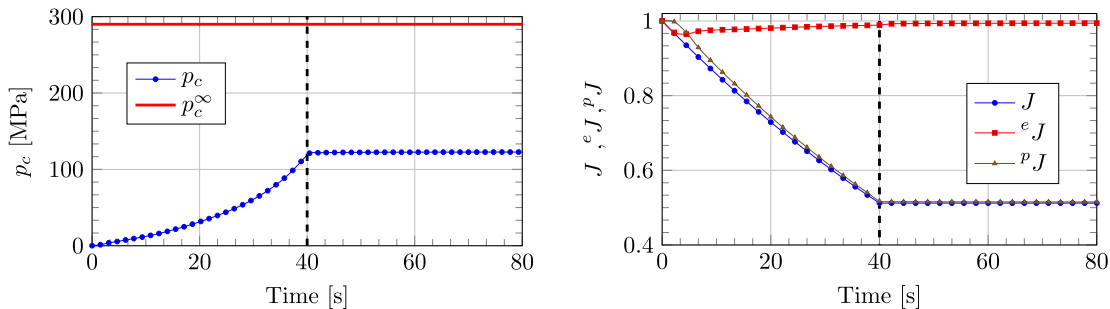


**Fig. 19.**  $p_c$  versus time (on the left) and the volumetric strains  $J$ ,  $e^J$ ,  $p^J$  versus time (on the right) for the complex loading case 1.

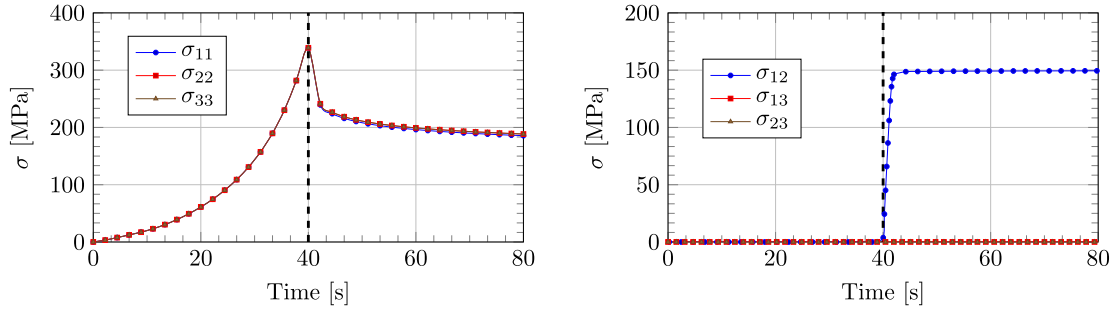


Fig. 20. The components of the Cauchy stresses as a function of the time for the complex loading case 1.

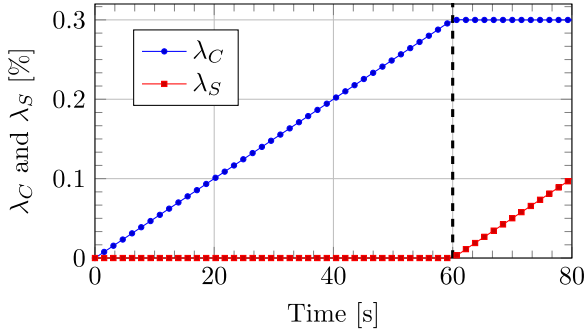


Fig. 21.  $\lambda_C$  and  $\lambda_S$  versus time for case 2.

**Algorithm 1** - Explicit integration algorithm.

- Compute the equivalent strain rates  $\dot{\gamma}_v$  and  $\dot{\gamma}_d$  at time  $t_n$  by Eqs. (19) and (20)
- Compute  ${}^p\mathbf{D}$  using  $\dot{\gamma}_v, \dot{\gamma}_d, \mathbf{S}_n$ , and  $p_{c_n}$  by Eq. (13)
- Compute  ${}^p\mathbf{F}_{n+1}$  using  ${}^p\mathbf{D}$  by Eq. (12)
- Compute  ${}^e\mathbf{F}_{n+1}$  using  $\mathbf{F}_{n+1}$  and  ${}^p\mathbf{F}_{n+1}$  by Eq. (1)
- Compute  $p_{c_{n+1}}$  using  ${}^p\mathbf{F}_{n+1}$  by Eq. (23)
- Update  $\mu, K, d$ , and  $c$  using Eqs. (7), (9), (8) and (11)
- Compute the stress  $\mathbf{S}_{n+1}$  using  ${}^e\mathbf{F}_{n+1}$  and  $p_{c_{n+1}}$  by Eq. (15)
- Compute the Kirchoff stress  $\boldsymbol{\tau}_{n+1}$  in Eq. (16)

**4. Numerical simulations**

Simulations are compared against experimental investigations on cold compacted copper powders, published by Carnavas and Page (1998), Bier et al. (2007), Bier (2008), Park et al. (1999), and Park (2007).

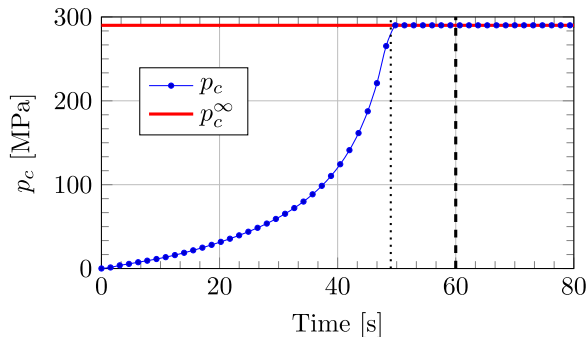


**Table 1**

Summary of material parameters.

Material parameters defining the hardening rule for $p_c$ , Eq. (23)	$a_1, a_2, \Lambda_1, \Lambda_2$
Material parameters defining $\mu$ , Eq. (7)	$\mu_0, \mu_1$
Material parameters defining $K$ , Eq. (11)	$p_0, \kappa$
Material parameters defining the transition variable $d$ , Eq. (9)	$B, p_{cb}$
Material parameters defining the cohesion $c$ , Eq. (8)	$c_\infty, \Gamma$
Power law exponent, Eq. (10)	$n$
Material parameters for the flow rule, Eqs. (19) and (20)	$\dot{\gamma}_0, m, M, \alpha$
Material parameters for the compaction function Eq. (18)	$g_0, p_c^\infty$

The calibration of material parameters is carried out in Section 4.1. In all sections that follow 4.1, we do not further calibrate any material parameters. Those simulations validate the capability of the model against different fields of interest.

**4.1. Material parameters calibration**

The material parameters that must be identified are summarized in the Table 1.

An experimental test generally employed to characterize the behavior of powders is the so-called die compaction test. It is a uniaxial constrained compression test (see Fig. 6), whose detailed description can be found in Cocks (2001) and in Bier (2008).

Bier et al. (2007) measured the axial and radial stresses for copper powder compounds at several loading rates. The axial stress is obtained as a function of the vertical displacement of the piston, after taking into account the deformation of the piston. Using their experimental results of the loading-unloading compaction test, the material parameters  $a_1, a_2, \Lambda_1$  and  $\Lambda_2$  were identified. Fig. 7(a) shows the least squares fit between experimental data and Eq. (23). Fig. 7(b) displays TMD as function of  $p_c$ . The change from

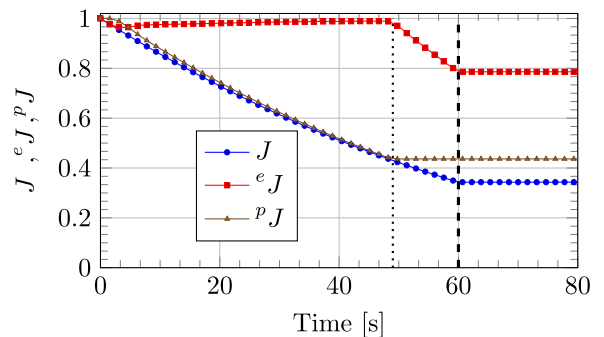


Fig. 22.  $p_c$  versus time (on the left) and the volumetric strains  $J, J^e, J^p$  versus time (on the right) for the complex loading case 2.

**Table 2**  
Material parameters calibrated for the copper powder.

Material parameters defining the hardening rule: $\ln(p^J) = f(p_c)$
$a_1 = 0.62, a_2 = 0.37, A_1 = 77.22 \text{ MPa}, A_2 = 13.01 \text{ MPa}$
Material parameters defining $\mu$ : $\mu_0 = 30 \text{ MPa}, \mu_1 = 60 [-]$
Material parameters defining $K$ : $p_0 = 0.063 \text{ MPa}, \kappa = 0.008 [-]$
Material parameters defining the transition variable $d$ : $B = 0.20 \text{ MPa}^{-1}, p_{cb} = 5.8 \text{ MPa}$
Material parameters defining the cohesion $c$ : $c_\infty = 15 \text{ MPa}, \Gamma = 0.01 \text{ MPa}^{-1}$
Power law exponent: $n = 2$
Material parameters for the flow rule: $\gamma_0 = 0.0005 \text{ s}^{-1}, m = 0.15, M = 1.0, \alpha = 1.1$
Material parameters for the compaction function: $g_0 = 1, p_c^\infty = 290 \text{ MPa}$

phase I to phase II is marked by the ‘break-point pressure’  $p_{cb}$ . The value of  $p_c^\infty$  corresponds to the value of  $p_c$  when TMD is equal to 100% and satisfies Eq. (26).

Initial TMD is taken from Bier et al. (2007),  $\text{TMD}_0 = 0.435$ . Next, we used least squares fit to calibrate  $\mu(p_c)$  and  $K(p_c)$  using Eq. (7) and Eq. (11), respectively, from experimental data taken from Carnavas and Page (1998). Figs. 8 and 9 show  $K$  and  $\mu$  as functions of TMD and  $p_c$ , respectively. The parameters for the cohesion  $c$  and for the transition parameter  $d$  are also identified using this data. The material parameters for the cohesion law should ideally be identified using direct experiments that allow evaluating the tensile strength as a function of the compaction state, such as the equi-biaxial flexure test (e.g. Bosi et al., 2014).

The parameters  $M$  and  $\alpha$  of the Cam–Clay model (Eq. (21)), which are used in our hardening functions,  $\bar{g}_\pi$  and  $\bar{g}_\tau$ , are identified using the data from Carnavas (1996), as shown in Fig. 10. The conversion of the data from the Cauchy stresses to Kirchhoff stresses is obtained using experimental data from Bier et al. (2007). The remaining parameters for the flow rule  $\gamma_0$  and  $m$ , are identified using the die compaction test at different strain rates.

#### 4.2. Simulation of the die compaction test

First, the die compaction test is simulated using material parameters listed in Table 2 to confirm their validity. The deformation gradient is assumed to be a known function of time

$$\mathbf{F}(t) = \begin{bmatrix} 1 - \lambda(t) & 0 & 0 \\ 0 & 1 & 0 \\ 0 & 0 & 1 \end{bmatrix}. \quad (27)$$

Two loading rates have been studied, i.e.  $\dot{\lambda} = 5.10^{-4} \text{ s}^{-1}$  and  $\dot{\lambda} = 5.10^{-3} \text{ s}^{-1}$ . Good comparison is found between the simulations and the experimental data provided in Bier et al. (2007), as plotted in Figs. 11 and 12.

The model captures the axial stress under a loading/unloading test with good accuracy, as seen in Fig. 13. The same figure shows that the hyperelastic behavior during unloading/reloading is captured well, which in turn validates the evolution of the material properties with the confining pressure  $p_c$ .

In order to predict the response once the material reaches the full solid state, we increased the deformation using several loading rates. Fig. 14 (a) and (b) reveal that the axial and radial stresses increase considerably. This behavior is related mainly due to the rise of pressure within the material, as shown in Fig. 15 (a). We note that for slow loading rates, the pressure rise is delayed compared to fast loading rates. However, all loading curves approach pressure insensitive (“limit”) behavior as  $p_c \rightarrow p_c^\infty$  for  $\lambda \approx 0.58$ . For a high applied pressure loading, the forming pressure (i.e., an internal variable) cannot overcome  $p_c^\infty$ . Thus, in view of Eq. (18)  $\beta_C = 0$  once  $p_c = p_c^\infty$  and the plastic flow becomes purely deviatoric (i.e.,

pressure independent). This implies that  $p^J$  remains constant and so does  $p_c$  (see Eq. (23)). As a consequence, neither the shear nor the bulk modulus increase further (see Eqs. (7) and (11)). Therefore, the shear stress magnitude in Eq. (16),  $\hat{\tau} = \|\text{dev}[\boldsymbol{\tau}]\|_{\mathcal{F}}$ , changes its trend and becomes almost constant when  $p_c$  reaches  $p_c^\infty$  (see Fig. 15 (b)). Due to the material viscosity, the higher the strain rate, the higher the value of  $\hat{\tau}$ .

#### 4.3. Simulation of tri-axial and bi-axial compression tests

Using the same set of parameters listed in Table 2, the model predicts the material response in the case of a bi-axial compression (see Fig. 16) and tri-axial compression tests (see Fig. 17). The deformation gradients are given by:

$$\mathbf{F}_B(t) = \begin{bmatrix} 1 - \lambda(t) & 0 & 0 \\ 0 & 1 - \lambda(t) & 0 \\ 0 & 0 & 1 \end{bmatrix},$$

$$\mathbf{F}_T(t) = \begin{bmatrix} 1 - \lambda(t) & 0 & 0 \\ 0 & 1 - \lambda(t) & 0 \\ 0 & 0 & 1 - \lambda(t) \end{bmatrix}.$$

Computations are compared to the work of Park et al. (1999) and Park (2007), who performed uniaxial strain, plain strain, and hydrostatic compression tests on copper powders. The loading rate is assumed to be very low in order to limit the effect of viscosity. Experimental results and model predictions are in good agreement.

#### 4.4. Combined compression and shear test

A tri-axial compaction is applied to the copper powder compacts followed by a simple shear deformation. Two loading cases are studied: (1) The density after compaction is below the full solid state. (2) The density equals the full solid material density at the end of the compaction. The amount of  $p_c$  distinguishes the two cases. The applied deformation gradient reads:

$$\mathbf{F}(t) = \begin{bmatrix} 1 - \lambda_C(t) & \lambda_S(t) & 0 \\ 0 & 1 - \lambda_C(t) & 0 \\ 0 & 0 & 1 - \lambda_C(t) \end{bmatrix}.$$

##### 4.4.1. Case of material density after compaction below the full solid state

The loading variables  $\lambda_C$  and  $\lambda_S$  are plotted as a function of the time in Fig. 18 for case (1). The compaction terminates at  $t = 40 \text{ s}$ . The final forming pressure  $p_c$  is below  $p_c^\infty$  (see Fig. 19). Therefore, the TMD is below 100%. After 40 s,  $p_c$  and  $p^J$  remain almost constant, as shown in Fig. 19. In terms of Cauchy stresses, a decrease in the values of components  $(\sigma_{11}, \sigma_{22}, \sigma_{33})$  is shown in Fig. 20, caused by the stress relaxation. The component  $\sigma_{12}$  increased, reaching the shear strength gained during the compaction process. A perfectly plastic like behavior has been obtained.

##### 4.4.2. Case of material density after compaction equal to the full dense state

The loading variables  $\lambda_C$  and  $\lambda_S$  are plotted as a function of the time in Fig. 21 for case (2). Fig. 22 shows that the value of  $p_c$  reached  $p_c^\infty$  before the end of the compression phase at  $t = 60 \text{ s}$ . After the full solid density is obtained, the value of  $p^J$  does not decrease further, as discussed in the simulation of the die compaction test in Section 4.2. Instead,  $e^J$  continues to decrease until the end of the compression stage (i.e. hyper-elastic compression between 40 and 60 s). This leads to high stress buildup in Fig. 23(left). In terms of Cauchy stress, the values of components  $(\sigma_{11}, \sigma_{22}, \sigma_{33})$  have no relaxation at the end of compression at  $t = 60 \text{ s}$ , as shown in Fig. 23 and are high due to the elastic compression as mentioned above. The component  $\sigma_{12}$  increases with  $\lambda_S$  until a saturation value corresponding to the final shear viscoplastic limit. The

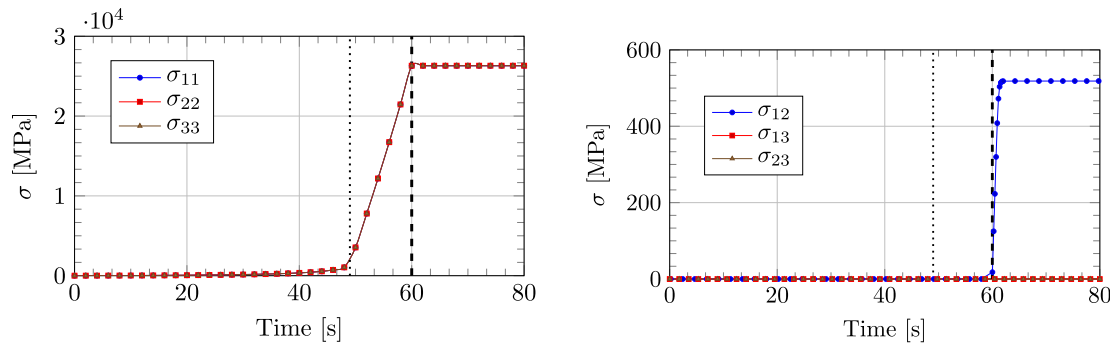


Fig. 23. The components of the Cauchy stress as a function of the time for the complex loading case 2.

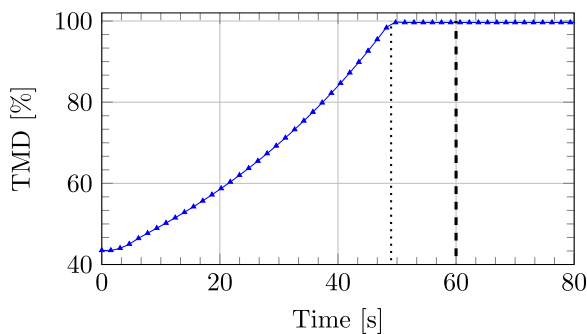


Fig. 24. TMD versus time for case 2.

steep slope of shear stress corresponds to a high shear modulus of a fully dense solid. Again, perfectly plastic like behavior has been obtained. Fig. 24 shows the evolution of the TMD versus time according to Eq. (26). 100% TMD is reached for  $p_c = p_c^\infty$ .

## 5. Conclusions

A novel phenomenological constitutive model for cold compacted materials has been developed. The transition of the material state from loose powder to full solid is described by three stages: granule sliding and rearrangement, granule deformation, and granule densification and hardening. The cohesion between the grains as well as the elastic properties are monotonically increasing as a function of an internal variable related to the forming pressure, which evolves with the irreversible volumetric change of the material. The model is expressed within the framework of large deformations, stemming from the multiplicative decomposition of the total deformation gradient into elastic and plastic parts. It couples pressure dependence and viscoplasticity under arbitrary loadings.

The proposed Helmholtz free energy resembles the classical neo-Hookean one. However, the elastic properties evolve with an internal variable, which corresponds to the exerted forming pressure (phenomena known as the *elasto-plastic coupling*). The plastic evolution is governed by rate-dependent, power-law flow rules for the volumetric and isochoric parts of the strain. The evolution of the forming pressure is related to the plastic deformation, which has a micro-mechanical nature.

An explicit numerical algorithm has been developed and implemented. Detailed model calibration has been described. Next, numerical predictions have been validated against experimental tests available in the literature on copper powders. Good agreement between model predictions and experimental results has been found, thus emphasizing the potential of the proposed model.

Simulations under complex loading histories, coupling triaxial pressure and shear, have shown the response of the model when the material density after compaction equals to that of a solid. In such a case, the final shear viscoplastic limit is reached and the cold-compacted powder behaves like a full solid material with a perfectly plastic response. A similar behavior in shear has been observed when compacting below the full solid state, namely a perfectly plastic like response at a shear stress level equal to the shear strength gained during the compaction process.

Complex micromechanical features such as grain crushing or particles densification have not been explicitly included in the model. Investigating those phenomena could enrich our phenomenological model, which is tailored for large industrial applications.

## Acknowledgments

This work was supported by the Department of Energy, National Nuclear Security Administration, under the award number DE-NA0002377 as part of the Predictive Science Academic Alliance Program II.

## References

- Areias, P., Matouš, K., 2008. Finite element formulation for modeling nonlinear viscoelastic elastomers. *Comput. Meth. Appl. Mech. Eng.* 197 (51), 4702–4717.
- Arzt, E., 1982. The influence of an increasing particle coordination on the densification of spherical powders. *Acta Metall.* 30 (10), 1883–1890.
- Aubertin, M., Li, L., 2004. A porosity-dependent inelastic criterion for engineering materials. *Int. J. Plast.* 20 (12), 2179–2208.
- Bakhshiani, A., Khoei, A., Mofid, M., 2004. A density-dependent endochronic plasticity for powder compaction processes. *Comput. Mech.* 34 (1), 53–66.
- Bažant, Z., Bhat, P., Shieh, C., 1976. Endochronic Theory for Inelasticity and Failure Analysis of Concrete Structures. Technical Report. Northwestern University doi:10.2172/7324674.
- Beaudoin, A., Acharya, A., 2001. A model for rate-dependent flow of metal polycrystals based on the slip plane lattice incompatibility. *Mater. Sci. Eng. A* 309–310 (Supplement C), 411–415. Dislocations 2000: An International Conference on the Fundamentals of Plastic Deformation. doi:10.1016/S0921-5093(00)01620-8.
- Bennett, K., Regueiro, R., Borja, R., 2016. Finite strain elastoplasticity considering the eshley stress for materials undergoing plastic volume change. *Int. J. Plast. Supplement C* 77, 214–245. doi:10.1016/j.ijplas.2015.10.007.
- Bier, W., 2008. A Constitutive Model for Metal Powder and Its Numerical Treatment Using Finite Elements. Kassel University Press GmbH.
- Bier, W., Dariel, M., Frage, N., Hartmann, S., Michailov, O., 2007. Die compaction of copper powder designed for material parameter identification. *Int. J. Mech. Sci.* 49 (6), 766–777.
- Bier, W., Hartmann, S., 2006. A finite strain constitutive model for metal powder compaction using a unique and convex single surface yield function. *Eur. J. Mech. A/Solids* 25 (6), 1009–1030.
- Bigoni, D., Piccolroaz, A., 2004. Yield criteria for quasibrittle and frictional materials. *Int. J. Solids Struct.* 41 (11), 2855–2878.
- Bosi, F., Piccolroaz, A., Gei, M., Dal Corso, F., Cocquiuo, A., Bigoni, D., 2014. Experimental investigation of the elastoplastic response of aluminum silicate spray dried powder during cold compaction. *J. Eur. Ceram. Soc.* 34 (11), 2633–2642.
- Carnavas, P., Page, N., 1998. Elastic properties of compacted metal powders. *J. Mater. Sci.* 33 (18), 4647–4655.

- Carnavas, P.C., 1996. The effect of particle morphology on metal powder compaction PhD thesis. University of Queensland.
- Cocks, A., Sinka, I., 2007. Constitutive modelling of powder compaction—i. theoretical concepts. *Mech. Mater.* 39 (4), 392–403.
- Cocks, A.C., 2001. Constitutive modelling of powder compaction and sintering. *Prog. Mater. Sci.* 46, 201–229.
- Cooper, A., Eaton, L., 1962. Compaction behavior of several ceramic powders. *J. Am. Ceram. Soc.* 45 (3), 97–101.
- Coube, O., Riedel, H., 2000. Numerical simulation of metal powder die compaction with special consideration of cracking. *Powder Metall.* 43 (2), 123–131.
- Doll, S., Schweizerhof, K., 2000. On the development of volumetric strain energy functions. *J. Appl. Mech.* 67 (1), 17–21.
- Drucker, D.C., Prager, W., 1952. Soil mechanics and plastic analysis or limit design. *Q. Appl. Math.* 10 (2), 157–165.
- Ehlers, W., 1995. A single-surface yield function for geomaterials. *Arch. Appl. Mech.* 65 (4), 246–259.
- Fleck, N., 1995. On the cold compaction of powders. *J. Mech. Phys. Solids.* 43 (9), 1409–1431.
- Fleck, N., Storåkers, B., McMeeking, R., 1997. The viscoplastic compaction of powders. In: IUTAM Symposium on Mechanics of Granular and Porous Materials. Springer, pp. 1–10.
- Fleck, N.A., Kuhn, L.T., McMeeking, R., 1992. Yielding of metal powder bonded by isolated contacts. *J. Mech. Phys. Solids* 40 (5), 1139–1162.
- German, R.M., 2005. *A-Z of Powder Metallurgy*. Elsevier Science Limited.
- Glass, S.J., Ewsuk, K.G., 1997. Ceramic powder compaction. *MRS Bull.* 22 (12), 24–28.
- Gu, C., Kim, M., Anand, L., 2001. Constitutive equations for metal powders: application to powder forming processes. *Int. J. Plast.* 17 (2), 147–209. doi:10.1016/S0749-6419(00)00029-2.
- Gurson, A.L., 1977. Continuum theory of ductile rupture by void nucleation and growth: part i—yield criteria and flow rules for porous ductile media. *J. Eng. Mater. Technol.* 99 (1), 2–15.
- Gurtin, M., Fried, E., Anand, L., 2010. *The Mechanics and Thermodynamics of Continua*. Cambridge University Press.
- Hägglblad, H.-Å., 1991. Constitutive models for powder materials. *Powder Technol* 67 (2), 127–137.
- Heyliger, P., McMeeking, R., 2001. Cold plastic compaction of powders by a network model. *J. Mech. Phys. Solids* 49 (9), 2031–2054.
- Iwashita, K., Oda, M., 1999. *Mechanics of Granular Materials: An Introduction*. CRC Press.
- Khoie, A., Azami, A., 2005. A single cone-cap plasticity with an isotropic hardening rule for powder materials. *Int. J. Mech. Sci.* 47 (1), 94–109.
- Khoie, A., Mofid, M., Bakhshiani, A., 2002. Modelling of powder compaction process using an endochronic plasticity model. *J. Mater. Process. Technol.* 130, 175–180.
- Kröner, E., 1959. Allgemeine kontinuumstheorie der versetzungen und eigenspannungen. *Arch. Ration. Mech. Anal.* 4 (1), 273–334.
- Kuhn, H., Downey, C., 1971. Deformation characteristics and plasticity theory of sintered powder materials. *Int. J. Powder Metall.* 7, 15–25.
- Lee, E.H., 1969. Elastic-plastic deformation at finite strains. *J. Appl. Mech.* 36 (1), 1–6.
- Matouš, K., Maniatty, A.M., 2004. Finite element formulation for modelling large deformations in elasto-viscoplastic polycrystals. *Int. J. Numer. Meth. Eng.* 60 (14), 2313–2333.
- Muzzio, F.J., Shinbrot, T., Glasser, B.J., 2002. Powder technology in the pharmaceutical industry: the need to catch up fast. *Powder Technol.* 124 (1), 1–7.
- Ogbonna, N., Fleck, N., 1995. Compaction of an array of spherical particles. *Acta Metall. Mater.* 43 (2), 603–620.
- Park, J., 2007. A yield function for copper powder in compaction. *J. Mater. Process. Technol.* 187, 672–675.
- Park, S.-J., Han, H.N., Oh, K.H., Lee, D.N., 1999. Model for compaction of metal powders. *Int. J. Mech. Sci.* 41 (2), 121–141.
- Piccolroaz, A., Bigoni, D., 2009. Yield criteria for quasibrittle and frictional materials: a generalization to surfaces with corners. *Int. J. Solids Struct.* 46 (20), 3587–3596.
- Piccolroaz, A., Bigoni, D., Gajo, A., 2006a. An elastoplastic framework for granular materials becoming cohesive through mechanical densification. Part I—small strain formulation. *European Journal of Mechanics-A/Solids* 25 (2), 334–357.
- Piccolroaz, A., Bigoni, D., Gajo, A., 2006b. An elastoplastic framework for granular materials becoming cohesive through mechanical densification. part II—the formulation of elastoplastic coupling at large strain. *Eur. J. Mech. A/Solids* 25 (2), 358–369.
- Schofield, A., Wroth, P., 1968. *Critical State Soil Mechanics*. McGraw-Hill London.
- Shima, S., Oyane, M., 1976. Plasticity theory for porous metals. *Int. J. Mech. Sci.* 18 (6), 285–291.
- Shuck, C.E., Frazee, M., Gillman, A., Beason, M.T., Gunduz, I.E., Matouš, K., Winarski, R., Mukasyan, A.S., 2016. X-ray nanotomography and focused-ion-beam sectioning for quantitative three-dimensional analysis of nanocomposites. *J. Synchrotron. Radiat.* 23 (4).
- Sinka, I., Cocks, A., 2007. Constitutive modelling of powder compaction—II. Evaluation of material data. *Mech. Mater.* 39 (4), 404–416.
- Sridhar, I., Fleck, N., 2000. Yield behaviour of cold compacted composite powders. *Acta Mater.* 48 (13), 3341–3352.
- Stupkiewicz, S., Piccolroaz, A., Bigoni, D., 2015. Finite-strain formulation and fe implementation of a constitutive model for powder compaction. *Comput. Meth. Appl. Mech. Eng.* 283, 856–880.
- Valanis, K., 1971. A theory of visco-plasticity with out a yield surface, part II application to mechanical behavior of metals. *Arch. Mech.* 23, 535–551.
- Watson, T., Wert, J., 1993. On the development of constitutive relations for metallic powders. *Metall. Trans. A* 24 (9), 2071–2081.
- Wei, Y., Anand, L., 2007. A constitutive model for powder-processed nanocrystalline metals. *Acta Mater.* 55 (3), 921–931. doi:10.1016/j.actamat.2006.09.014.
- Yi, Y.B., Wang, C.W., Sastry, A.M., 2005. Compression of packed particulate systems: simulations and experiments in graphitic li-ion anodes. *J. Eng. Mater. Technol.* 128 (1), 73–80.